A comparative study of subgrid scale models for the prediction of transition in turbulent boundary layers

By T. Sayadi AND P. Moin

1. Motivation and objectives

Flow parameters such as skin friction and heat transfer coefficient are directly affected by the transition phenomenon. Therefore, the ability to predict the "point" of transition and to capture the physics of non-linear interactions up to the stage where the flow becomes fully turbulent is of great interest.

The transition process of an incompressible boundary layer has been widely studied both experimentally and numerically (see Kachanov (1994) for a comprehensive review). Most of the numerical attempts to simulate transition were based on the temporal model (Wray & Hussaini 1984). In this approach the temporal growth of each mode at a specified stream-wise location along the boundary layer is predicted. Since the boundary layer grows in space, a more realistic way of studying the process of transition numerically is to allow the flow and the disturbances to evolve downstream. One disadvantage of spatially evolving simulation is that it is computationally more expensive than a temporal one. Direct numerical simulation (DNS) of transition on a flat plate boundary layer although feasible, is quite costly especially if the turbulent regime after the transition process is to be captured accurately. As an example, Wu & Moin (2009) computed by-pass transition induced by free stream turbulence using a total of approximately 200 million grid points. On the other hand, Reynolds-averaged Navier-Stokes equations (RANS) calculations have not been predictive as they rely on the *a priori* knowledge of the location of the point of transition.

The objective of this study is to assess the predictive capability of large eddy simulation (LES) for laminar/turbulent transition using the dynamic subgrid scale (SGS) models. LES has been applied as a tool for predicting transition, by Huai *et al.* (1997) for example. However, the performance of SGS models has not been directly assessed.

Transition consists of different stages. In the natural transition of an incompressible boundary layer, which is well understood, the first stage consists of the exponential growth of the two-dimensional Tollmein-Schlichting (TS) wave. In the next stage, this mode interacts with modes of different frequencies and produces other modes with smaller scales. This non-linear interaction causes secondary instabilities and eventually leads to the break down to turbulence. If LES is to be applied successfully to this transition scenario it needs to adapt to each of these stages in order to capture the physics accurately. In the linear and early non-linear stages the turbulence model should be inactive to allow the disturbances to grow according to the linear stability theory. The model should become active gradually in the late stages of transition and the early turbulence regime.

In this study we assess the performance of three different SGS models in predicting transition:

(a) Dynamic Smagorinsky eddy viscosity model (Smagorinsky 1963),

(*b*) Dynamic scale similarity (Erlebacher *et al.* 1992),

(*c*) Dynamic one equation model, based on the derived transport equation for the SGS kinetic energy (Ghosal *et al.* 1995).

These models are evaluated based on their prediction of the skin friction coefficient in a simulation of a transitional and turbulent boundary layer up to $Re_\theta = 1300$.

2. Governing equations

Favre averaged compressible Navier-Stokes equations are solved numerically:

$$\frac{\partial \overline{\rho}}{\partial t} + \frac{\partial \overline{\rho}\widetilde{u_j}}{\partial x_j} = 0, \tag{2.1}$$

$$\frac{\partial \overline{\rho}\widetilde{u_i}}{\partial t} + \frac{\partial \overline{\rho}\tilde{u}_j\tilde{u}_i}{\partial x_j} = -\frac{\partial \overline{p}}{\partial x_i} + \frac{\partial \widetilde{\sigma_{ij}}}{\partial x_j} - \frac{\partial \tau_{ij}^{sgs}}{\partial x_j}, \tag{2.2}$$

$$\frac{\partial \overline{E}}{\partial t} + \frac{\partial \overline{(E+p)}\widetilde{u_j}}{\partial x_j} = \frac{\partial}{\partial x_j}\left(\kappa \frac{\partial \overline{T}}{\partial x_j}\right) + \frac{\partial}{\partial x_j}\left(\tilde{u}_i\widetilde{\sigma_{ij}}\right) - \frac{\partial}{\partial x_j}(q_j^{sgs}). \tag{2.3}$$

In the above set of equations E is the total energy and $\widetilde{\sigma_{ij}} = \tilde{\mu}\left(\frac{\partial \tilde{u}_i}{\partial x_j} + \frac{\partial \tilde{u}_j}{\partial x_i} + \frac{2}{3}\frac{\partial \tilde{u}_k}{\partial x_k}\right)$ is the resolved stress tensor. τ_{ij}^{sgs} and q_j^{sgs} are the unresolved stress and heat fluxes and are defined as follows:

$$\tau_{ij}^{sgs} = \overline{\rho}(\widetilde{u_i u_j} - \tilde{u}_i\tilde{u}_j), \tag{2.4}$$

$$q_j^{sgs} = \overline{\rho}(\widetilde{Tu_j} - \tilde{T}\tilde{u}_j). \tag{2.5}$$

The three SGS models that are used to close the above equations are presented below:

2.1. *Dynamic Smagorinsky*

The dynamic subgrid scale model for compressible flows of Moin *et al.* (1991) for subgrid scale stress and heat flux are defined as:

$$\tau_{ij}^{sgs} - 1/3\delta_{ij}\tau_{kk}^{sgs} = -2C\overline{\Delta}^2\overline{\rho}|\widetilde{S}|(\widetilde{S_{ij}} - 1/3\widetilde{S_{kk}}\delta_{ij}), \tag{2.6}$$

$$\tau_{kk}^{sgs} = 2C_I\overline{\rho}\overline{\Delta}^2|\widetilde{S}|^2, \tag{2.7}$$

$$q_j^{sgs} = -\frac{\overline{\rho}\nu_t}{Pr_t}\frac{\partial \tilde{T}}{\partial x_j}, \tag{2.8}$$

and ν_t is defined as $C\overline{\Delta^2}\overline{\rho}|\widetilde{S}|$, and $|\widetilde{S}| = \sqrt{2\widetilde{S_{ij}}\widetilde{S_{ij}}}$.

Constants, C, C_I and $1/Pr_t$ are then calculated dynamically using the Germano identity. Averaging in the homogeneous (spanwise) direction is applied to stabilize the calculation of the coefficients.

2.2. *Dynamic scale similarity*

Subgrid scale stress is decomposed into three Galilean-invariant parts:

$$\tau_{ij}^{sgs} = L_{ij} + C_{ij} + R_{ij}. \tag{2.9}$$

The first term on the right-hand side of the above equation represents the Leonard stress, the second the cross stress and the last term the SGS Reynolds stress. All these terms

are presented based on Favre filtering below:

$$L_{ij} = \overline{\rho}(\widetilde{\widetilde{u_i}\widetilde{u_j}} - \tilde{\widetilde{u}}_i\tilde{\widetilde{u}}_j), \tag{2.10}$$

$$C_{ij} = \overline{\rho}(\widetilde{\widetilde{u_i}u_j'} + \widetilde{u_i'\widetilde{u_j}} - \tilde{\widetilde{u}}_i\tilde{u_j'} - \tilde{u_i'}\tilde{\widetilde{u}}_j), \tag{2.11}$$

$$R_{ij} = \overline{\rho}(\widetilde{u_i'u_j'} - \tilde{u_i'}\tilde{u_j'}). \tag{2.12}$$

The Leonard stress can be estimated by defining a filter that represents the grid filter. Reynolds and cross stresses are then modeled using compressible generalization of the Smagorinsky model. Following this procedure leads to the following formulation of the SGS stress:

$$\tau_{ij}^{sgs} - 1/3\delta_{ij}\tau_{kk}^{sgs} = \overline{\rho}L_{ij}^* - 2C\overline{\Delta}^2\overline{\rho}|\widetilde{S}|(\widetilde{S_{ij}} - 1/3\widetilde{S_{kk}}\delta_{ij}), \tag{2.13}$$

where L_{ij}^* is the trace free part of the Leonard stress tensor. τ_{kk}^{sgs} is modeled the same way as in Eqn. 2.7. The subgrid scale heat flux can be decomposed in the same fashion as the subgrid scale stress (Erlebacher *et al.* 1992),

$$q_j^{sgs} = Q^{(L)} + Q^{(C)} + Q^{(R)}, \tag{2.14}$$

where, the first term on the right-hand side is the Leonard heat flux; the second term the cross, and the third term the Reynolds heat fluxes. They are defined as:

$$Q_j^{(L)} = \overline{\rho}(\widetilde{\tilde{T}\tilde{u}_j} - \tilde{\tilde{T}}\tilde{\tilde{u}}_j), \tag{2.15}$$

$$Q_j^{(C)} = \overline{\rho}(\widetilde{\tilde{T}u_j'} + \widetilde{T'\tilde{u}_j} - \tilde{\tilde{T}}\tilde{u_j'} - \tilde{T'}\tilde{\tilde{u}}_j), \tag{2.16}$$

$$Q_j^{(R)} = \overline{\rho}(\widetilde{T'u_j'} - \tilde{T'}\tilde{u_j'}). \tag{2.17}$$

The Leonard heat flux can be computed directly choosing a filter to represent the grid filter. The cross and Reynolds stresses can be approximated the same way as described in Section 2.1, and the overall model for the SGS heat flux is written as:

$$q_j^{sgs} = \overline{\rho}(\widetilde{\tilde{T}\tilde{u}_j} - \tilde{\tilde{T}}\tilde{\tilde{u}}_j) - \frac{\overline{\rho}\nu_t}{Pr_t}\frac{\partial\tilde{T}}{\partial x_j} \tag{2.18}$$

2.3. *Dynamic one equation model*

This model was proposed by Ghosal *et al.* (1995) for incompressible turbulence, and we have extended the model to a compressible framework. Consider the unfiltered momentum equation,

$$\frac{\partial\rho u_i}{\partial t} + \frac{\partial\rho u_i u_j}{\partial x_j} = -\frac{\partial p}{\partial x_i} + \frac{\partial\sigma_{ij}}{\partial x_j}, \tag{2.19}$$

where σ_{ij} is the total stress. Multiplying the above equation by u_i, using continuity and finally filtering the resulting equation yields,

$$\frac{\partial\overline{\rho}\widetilde{\frac{u_i^2}{2}}}{\partial t} + \frac{\partial\overline{\rho}\widetilde{u_j}\widetilde{\frac{u_i^2}{2}}}{\partial x_j} = \overline{-u_i\frac{\partial p}{\partial x_i}} + \overline{u_i\frac{\partial\sigma_{ij}}{\partial x_j}} + \frac{\partial}{\partial x_j}\left(\overline{\rho}\widetilde{u_j}\widetilde{\frac{u_iu_i}{2}} - \overline{\rho u_j\frac{u_i^2}{2}}\right). \tag{2.20}$$

Multiplying both sides of Eqn. 2.2 by $\widetilde{u_i}$, and using Eqn. 2.1 gives:

$$\frac{\partial\overline{\rho}\widetilde{\frac{u_i}{2}}^2}{\partial t} + \frac{\partial\overline{\rho}\widetilde{u_j}\widetilde{\frac{u_i}{2}}^2}{\partial x_j} = -\widetilde{u_i}\frac{\partial\overline{p}}{\partial x_i} + \widetilde{u_i}\frac{\partial\widetilde{\sigma_{ij}}}{\partial x_j} - \widetilde{u_i}\frac{\partial\tau_{ij}^{sgs}}{\partial x_j}. \tag{2.21}$$

Finally the transport equation for SGS kinetic energy is derived by subtracting Eqn. 2.21 from Eqn. 2.20 (Chai & Mahesh 2010):

$$\begin{aligned}\frac{\partial \overline{\rho} k^{sgs}}{\partial t}+\frac{\partial \overline{\rho}\widetilde{u_j}k^{sgs}}{\partial x_j} =& -\tau_{ij}^{sgs}\frac{\partial \widetilde{u_i}}{\partial x_j}+\frac{\partial}{\partial x_j}\left(\tilde{\mu}\frac{\partial k^{sgs}}{\partial x_j}\right)\\ &+\frac{\partial}{\partial x_j}\left[\frac{1}{2}\overline{\rho}(\widetilde{u_i^2}\tilde{u_j}-u_i\widetilde{u_i}u_j)+\frac{1}{3}\left(\overline{\mu u_j\frac{\partial u_k}{\partial x_k}}-\tilde{\mu}\tilde{u_j}\frac{\partial \tilde{u_k}}{\partial x_k}\right)+\tilde{u_i}\tau_{ij}^{sgs}\right]\\ &+\frac{\partial}{\partial x_j}\left[\overline{\mu\frac{\partial (u_i^2)/2}{\partial x_j}}-\tilde{\mu}\frac{\partial(\widetilde{u_iu_i}/2)}{\partial x_j}\right]\\ &-\left(\overline{u_i\frac{\partial p}{\partial x_i}}-\widetilde{u_i}\frac{\partial \overline{p}}{\partial x_i}\right)\\ &-\left(\overline{\mu\frac{\partial u_i}{\partial x_j}\frac{\partial u_i}{\partial x_j}}-\tilde{\mu}\frac{\partial \tilde{u_i}}{\partial x_j}\frac{\partial \tilde{u_i}}{\partial x_j}\right)-\frac{1}{3}\left[\overline{\mu\left(\frac{\partial u_k}{\partial x_k}\right)^2}-\tilde{\mu}\left(\frac{\partial \tilde{u_k}}{\partial x_k}\right)^2\right]\\ &+\left[\overline{\left(u_i\frac{\partial u_j}{\partial x_i}-u_j\frac{\partial u_k}{\partial x_k}\right)\frac{\partial \mu}{\partial x_j}}-\left(\tilde{u_i}\frac{\partial \tilde{u_j}}{\partial x_i}-\tilde{u_j}\frac{\partial \tilde{u_k}}{\partial x_k}\right)\frac{\partial \tilde{\mu}}{\partial x_j}\right],\end{aligned}$$

where SGS kinetic energy is $\overline{\rho}k^{sgs}=\frac{1}{2}\overline{\rho}(\widetilde{u_iu_i}-\tilde{u_i}\tilde{u_i})=\frac{1}{2}\tau_{ii}^{sgs}$. The first term on the right-hand side is the production term; the second term is the molecular diffusion; the third and fourth terms are the turbulent diffusion; the fifth term contains the pressure dilatation which is neglected in this study but could be of substantial value, and it can be modeled using the approach of Chai & Mahesh (2010); the sixth term is the SGS dissipation; the seventh term can be neglected in case of an incompressible flow. This assumption is plausible here since the Mach number is 0.2. However, as Chai & Mahesh (2010) apply this model to a normal shock/isotropic turbulence interaction of a Mach number of 1.5 and turbulent Mach number of 0.221, this term is of great importance and they model it using the dynamic procedure. The other terms are neglected for simplicity. The turbulent diffusion is modeled by a constant, D_t, that is calculated dynamically. The dissipation term is approximated by the constant C^*, which is also calculated dynamically. Therefore, the modeled transport equation for SGS kinetic energy can be written as:

$$\frac{\partial \overline{\rho}k^{sgs}}{\partial t}+\frac{\partial(\overline{\rho}\tilde{u}_jk^{sgs})}{\partial x_j}=-\tau_{ij}^{sgs}\frac{\partial \tilde{u}_i}{\partial x_j}+\frac{\partial}{\partial x_j}\left(\tilde{\mu}\frac{\partial k^{sgs}}{\partial x_j}\right)+\frac{\partial}{\partial x_j}\left(D_t\frac{\partial k^{sgs}}{\partial x_j}\right)-\overline{\rho}C^*\frac{(k^{sgs})^{\frac{3}{2}}}{\overline{\Delta}}. \tag{2.22}$$

In the equation above, $\overline{\Delta}$ is the grid filter width. C^* and D_t are both non-negative dimensional coefficients that vary in space and time.

Finally in the one equation model

$$\tau_{ij}^{sgs}-\frac{2}{3}\delta_{ij}\overline{\rho}k^{sgs}=-2C\overline{\Delta}\overline{\rho}(k^{sgs})^{\frac{1}{2}}(\widetilde{S_{ij}}-\frac{1}{3}\widetilde{S_{kk}}\delta_{ij}), \tag{2.23}$$

where C is obtained dynamically. The SGS heat flux is defined in the same way as in Eqn. 2.8.

3. Numerical method and validation case

Compressible Navier-Stokes equations are solved for a perfect gas using sixth-order compact finite differences. The details of this algorithm is described in Nagarajan *et*

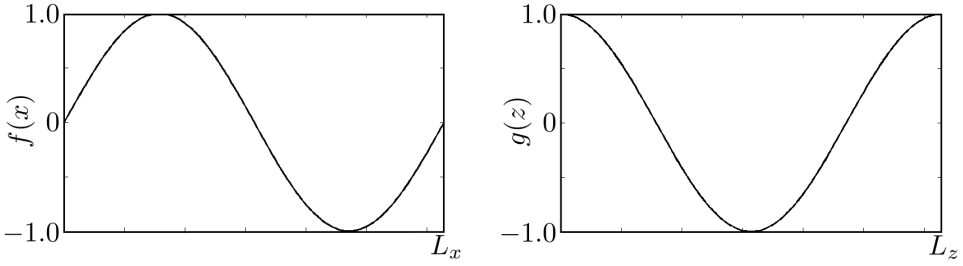

FIGURE 1. Modulation functions for the wall-normal velocity boundary condition in Eqn. 3.1, L_x and L_z are the wavelengths of the unstable wave along the stream-wise and span-wise directions.

al. (2004). An implicit-explicit time advancing scheme is applied. For the explicit time advancement a RK3 scheme is employed and a second order A-stable scheme is used for the implicit portion. The numerical scheme is constructed on a structured curvilinear grid, and the variables are staggered in space. The Mach number is chosen to be 0.2.

The experiment of Kachanov & Levchenko (1984) was chosen to validate the results. This experiment was conducted in a low-turbulence wind tunnel. The speed of air in the free-stream was fixed at $U_\infty = 9.18$ m/s, and turbulence intensities were less than 0.02%. The flat plate was mounted horizontally in the test section under zero angle of attack. The model had essentially zero pressure gradient except close to the leading edge. Sinusoidal disturbances of Tollmien-Schlichting waves were introduced into the laminar boundary layer by a vibrating ribbon. The ribbon was located 250 mm downstream of the leading edge and at the height of 0.15-0.2 mm from the surface of the plate.

3.1. *Boundary conditions*

The TS wave and subharmonic wave are introduced into the domain at the wall. Normal velocity at this location was prescribed as the blowing and suction boundary condition of Haui *et al.* (1997). The blowing and suction introduces no mass into domain. It aims at reproducing the effect of the vibrating ribbon in the experiment via a wall-normal velocity of the form:

$$v(x,z,t) = A_1 f(x)\sin(\omega t) + A_{1/2} f(x) g(z)\cos(\frac{\omega}{2}t + \phi). \tag{3.1}$$

A_1 and $A_{1/2}$ are the disturbance amplitudes of first and subharmonic waves respectively, and ϕ is the phase shift between the two. These values have been chosen such that the initial receptivity process matches the experiment. f and g are modulation functions and are shown in Figure 1.

The plate is treated as an adiabatic wall. Periodic boundary conditions are used along the span-wise and stream-wise directions. Because the boundary layer is spatially growing, use of a stream-wise periodic boundary condition requires that the profile be reshaped at the end of the domain to match the inflow profile calculated from the similarity solution of the laminar compressible boundary layer. This reshaping procedure is performed inside the sponge region (see Figure 2). This method was used successfully by Spalart & Watmuff (1993) in a numerical simulation of a turbulent boundary layer. It was demonstrated that solution of the Navier-Stokes equation is accurate outside of the sponge region despite the periodic boundary condition used along the inhomogenous stream-wise direction.

Sponges used at the boundaries, minimize the effect of numerical disturbances reflected into the domain.

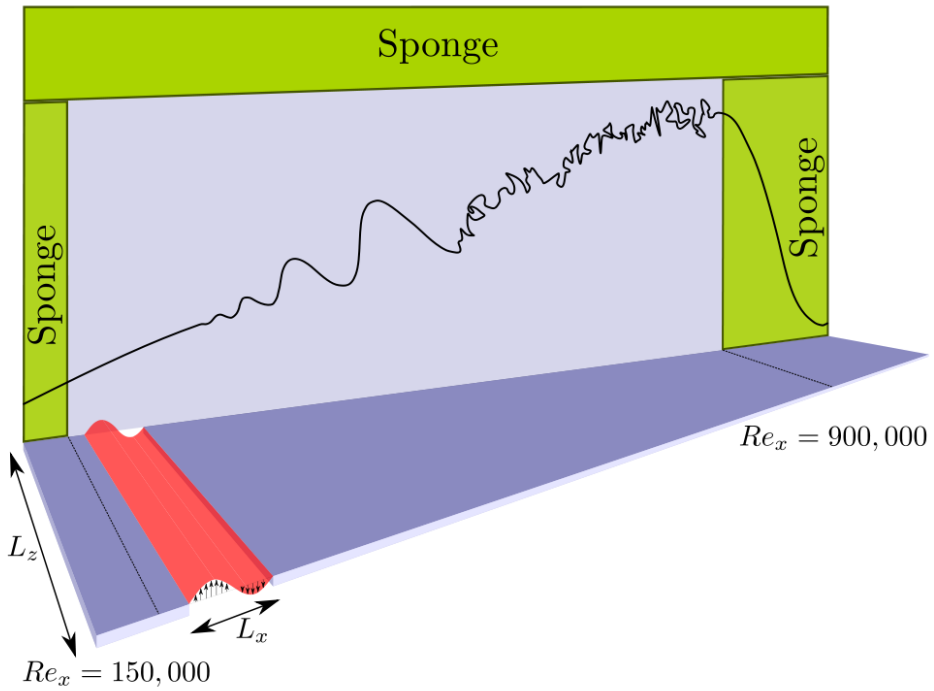

FIGURE 2. Computational domain. The solid line schematically shows the edge of the boundary layer.

Case	Grid points	Δx^+	Δy^+	Δz^+	L_x/δ_{99}	L_y/δ_{99}	L_z/δ_{99}
a	960x160x64	32	0.7	7	64	3.3	1.05
b	480x160x32	64	0.7	14	64	3.3	1.05
c	960x160x32	32	0.7	14	64	3.3	1.05
d	960x160x16	32	0.7	28	64	3.3	1.05
e	480x160x16	64	0.7	28	64	3.3	1.05

TABLE 1. Characteristics of the different grids. δ_{99} is the boundary layer thickness calculated at $Re_x = 9 \times 10^5$.

4. Computational Domain

The computational domain is shown in Figure 2. It extends from $Re_x = 10^5$ to $Re_x = 10^6$, the location of the disturbance strip is at $Re_x = 1.6 \times 10^5$ and it extends for $\Delta Re_x = 0.15 \times 10^5$. The sponge in the stream-wise direction starts at $Re_x = 9.1 \times 10^5$ and extends to the end of the computational domain. The sponge at the inflow extends up to $Re_x = 1.5 \times 10^5$. The sponge in the wall-normal direction has a thickness of $L = \delta_{99}$, where δ_{99} is the boundary layer thickness at $Re_x = 9 \times 10^5$.

The grids used in this study are shown in Table 1 along with the dimensions of the numerical domain. The largest grid consists of eight million grid points and the smallest grid uses one million. The wall units are calculated based on the turbulent shear velocity at $Re_x = 9 \times 10^5$, close to the end of the physical domain.

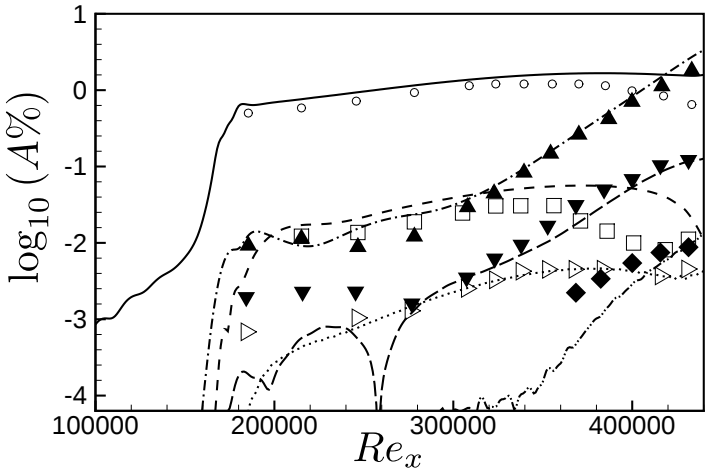

FIGURE 3. Percentage of disturbance amplitudes relative to free-stream velocity. Numerical (lines) and experimental (symbols) results. ω: solid line and circles, 2ω: dashed line and squares, 3ω: dotted line and right triangles $\frac{\omega}{2}$: dashed-dotted line and triangles, $\frac{3\omega}{2}$: long dashed line and gradient, $\frac{5\omega}{2}$: double dotted-dashed line and diamonds.

5. Results

The constant coefficient Smagorinsky model is unsatisfactory when applied to a flow undergoing transition because it fails to differentiate between laminar and turbulent flow, and turbulent viscosity remains active throughout the whole domain. This causes the disturbances to dissipate at the beginning of transition and the point of transition is not predicted accurately. Here we applied the dynamic procedure which is expected to be inactive in the smooth flow regions.

The evolutions of different modes (for example fundamental, ω and subharmonic, $\frac{\omega}{2}$) are shown in Figure 3. These results are from the Fourier analysis of two periods of fundamental harmonic, collected ten periods after the disturbance was initiated. The figure shows the spatial growth of typical wave components of the stream-wise velocity. The results are compared to the experiment, and are represented in the figure by symbols. The modes are calculated at a constant wall distance of $y/\delta = 0.26$, as is done in the experiment. There is very good agreement with the amplitudes, calculated experimentally, up to the end of the domain where the numerical results start to deviate from experimental values. This is not surprising since in the numerical calculation only the second and first harmonics are introduced into the domain through the blowing and suction, whereas in the experiment all modes are present. Therefore, the nonlinear interactions at the end of the domain can be affected. On the other hand, the sudden decay of the modes could be the effect of adverse pressure gradient present in the experiment. In the DNS (Fasel *et al.* 1990) of the same experiment the decay of the modal amplitudes was also not observed. As can be concluded from the figure, through dynamic procedure the growth rates at the start of transition are not affected by the dynamic Smagorinsky model. This can be explained by the value of turbulent viscosity being close to zero in this region. The same is true for the other two dynamic models investigated in this study.

The goal of this study is to evaluate LES on grids that are as coarse as possible. To verify how coarse the grid can become before the model fails, the dynamic Smagorinsky

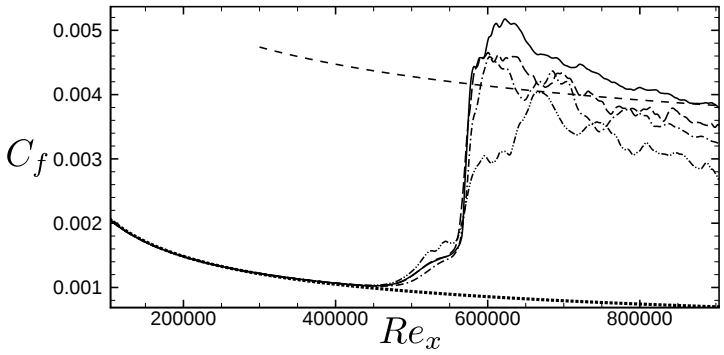

FIGURE 4. Skin friction coefficient for four different grid resolutions with dynamic Smagorinsky model, laminar correlation: dotted line, turbulent correlation $C_f \approx (0.455)/(\ln(0.06Re_x))^2$ (White 1991): dashed line, case(a): solid line, case(b): dashed-dotted line, case (c): long dashed line, case(d): dashed-double-dotted line.

model is applied to four different grid resolutions, shown in Table 1 as cases (a), (b), (c), and (d). The performance of the model is assessed by comparing the resulting skin friction profile with the laminar and turbulent correlations. In the case of subharmonic transition, an overshoot in the skin friction coefficient from the turbulent correlation is expected (Dhawan & Narasimha 1957). This overshoot happens at late stages of transition and the profile converges to the expected turbulent value later as turbulence develops. As can be seen in Figure 4, the finest grid shows the expected overshoot and downstream the skin friction profile converges to the nominal turbulent value. However, as the grid gets coarser the models performance deteriorates in predicting the skin friction profile. The point of transition is usually defined as the location where value of the skin friction coefficient diverges from the laminar value. LES prediction of the "point" of transition seems to be adequate for all the grids considered with higher grid resolution cases showing better convergence throughout the process.

Two other SGS model were applied to the same transition scenario. These models were described in Section 2. The performance of these three SGS models are compared using the grid described in Table 1 as case (e). This grid is the coarsest grid among the five employed in this study. There are 16 points along the span-wise direction and 480 in the stream-wise direction. These models produce different levels of turbulent viscosity as is shown in Figure 5. In this figure the contours of turbulent viscosity are time averaged and span-wise averaged. They are normalized by the physical kinematic viscosity. All three models seem to be activated in the same vicinity (transition), but the magnitudes of the corresponding eddy viscosities are different. The maximum value of the eddy viscosity for dynamic one equation model is 3.5, for dynamic Smagorinsky model it is 1.8. It is 1.2 in the case of the dynamic scale similarity model. The eddy viscosity model in this case represents only part of the subgrid stress, and therefore this value is expected to be lower.

The models were then compared through the skin friction profile generated in each case. The results are shown in Figure 6. The initial stage of transition where the skin friction profile starts to deviate from the laminar correlation is slightly affected by the choice of the model. The dynamic one equation model predicts earlier transition than the dynamic Smagorinsky model and the dynamic scale similarity model. However, all

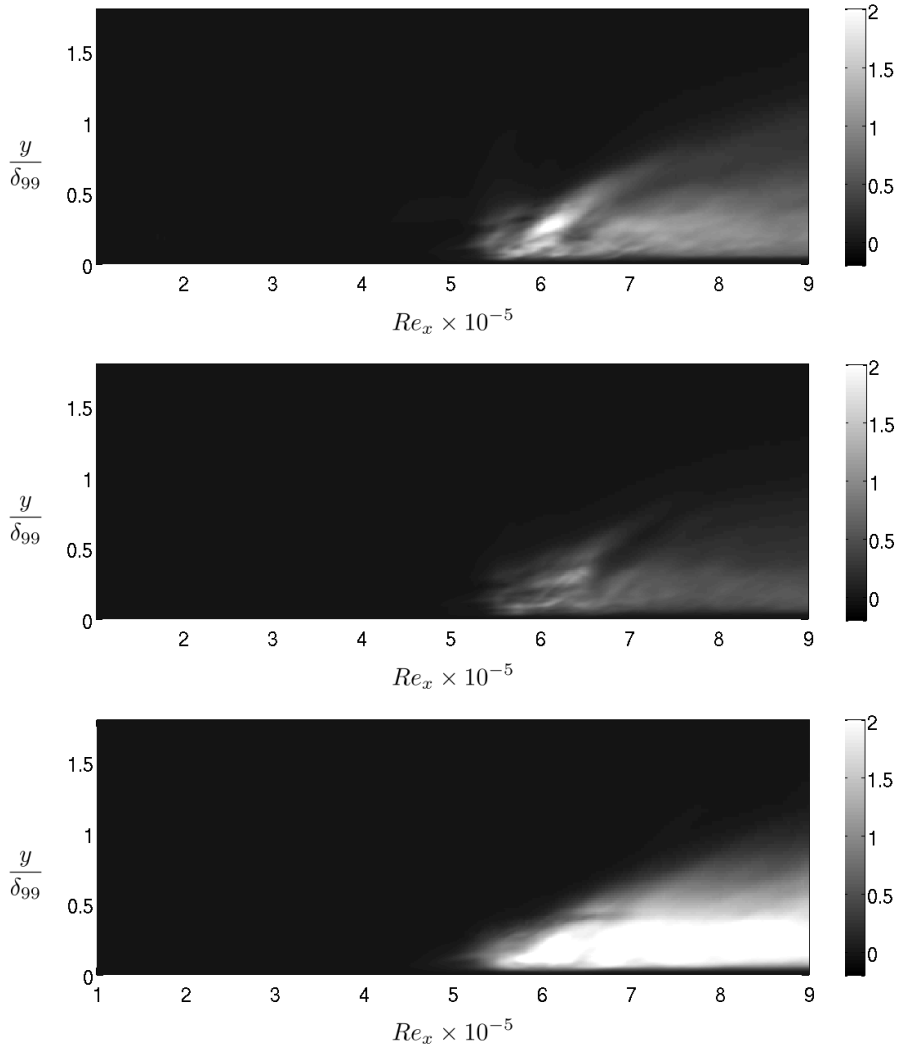

FIGURE 5. Contours of normalized turbulent viscosity. Dynamic Smagorinsky: (top), dynamic scale similarity: (middle), dynamic one equation model: (bottom).

models underpredict the overshoot and the turbulent correlation as the boundary layer becomes turbulent. The skin friction coefficients are also compared to a case which is simulated on the same grid resolution without an SGS model. This case is called the no model case. It is deduced from Figure 6 that the no model case predicts the start of transition later than simulations with an SGS model. On the other hand, its performance is the same as the cases with SGS models in the late transition and turbulent regime, as far as the prediction of the skin friction is concerned. Prediction of the normalized turbulent intensities are shown in Figure 7. The results are compared to the DNS of Wu & Moin (2009) at the same location of $Re_\theta = 1300$.

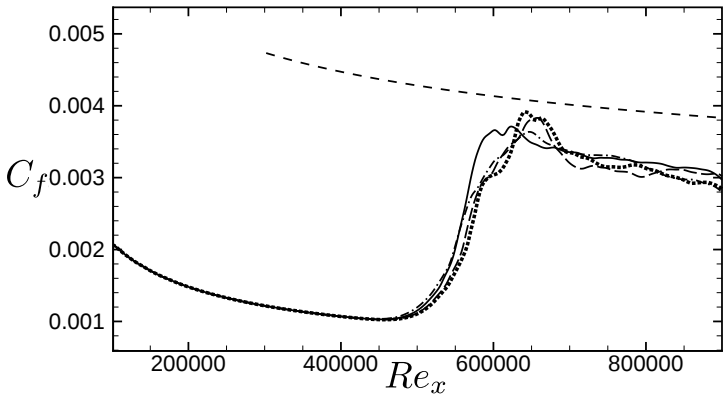

FIGURE 6. Skin friction coefficient using the three SGS models, turbulent correlation $C_f \approx (0.455)/(\ln(0.06Re_x))^2$ (White 1991): dashed line, dynamic Smagorinsky: solid line, dynamic one equation model: dashed-dotted line, dynamic scale similarity: long dashed line, no model: dotted line.

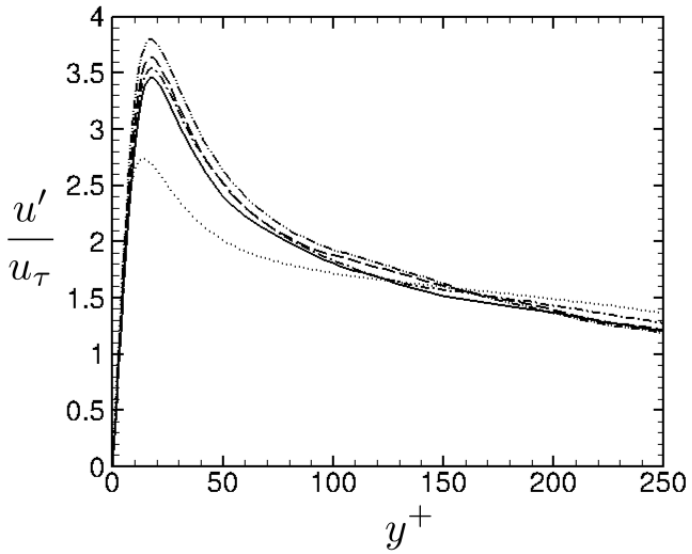

FIGURE 7. Stream-wise turbulent intensities for the three SGS models, DNS Wu and Moin (2009): dotted line, dynamic Smagorinsky: solid line, dynamic one equation model: dashed-dotted line, dynamic scale similarity: long dashed line, no model: dashed-double-dotted line.

6. Summary and conclusions

Using three subgrid scale models using the dynamic procedure, it was demonstrated that turbulent viscosity in the laminar and early transition is close to zero, and therefore the linear stage of transition is resolved directly and growth rates of the relevant modes match the experimental values. Applying dynamic Smagorinsky to different grid resolutions demonstrates that as the grid gets coarser the skin friction profile deviates from its true value and in the case of very coarse grids, the overshoot and skin friction in

the downstream turbulence are both underpredicted. the dynamic one equation model, dynamic scale similarity and dynamic Smagorinsky were all applied to the grid with the lowest resolution and their results were compared. All the cases underpredict the overshoot in the skin friction profile at the end of transition. At this very coarse resolution there is also no improvement in predicting the turbulent skin friction values by using different or no models.

The asymptotic behavior of the skin friction coefficient for this particular transition scenario has not been reported, therefore DNS of the same configuration is currently underway. After the skin friction profile is determined the performance of each model will be better quantified.

Acknowledgment

Financial support from the Department of Energy under the PSAAP program is gratefully acknowledged.

REFERENCES

Chai X. & Mahesh K. 2010 Dynamic k-equation model for large eddy simulation of compressible flows. *AIAA* 2010-5026.

Dhawan S. & Narasimha R. 1957 Some properties of boundary layer flow during the transition from laminar to turbulent motion. *J. Fluid Mech.* **3**, 418-436.

Erlebacher G., Hussaini M. Y., Speziale C. G., & Zang T. A. 1992 Toward the large-eddy simulation of compressible turbulent flows. *J. Fluid Mech.* **238**, 155-185

Fasel H. F., Rist U., & Konzelmann U. 1990 Numerical investigation of three-dimensional development in boundary-layer transition, *AIAA* **28**, No. 1, 29-37

Ghosal S., Lund T. S., Moin P., & Akselvoll K. 1995 A dynamic localization model for large-eddy simulation of turbulent flows. *J. Fluid Mech.* **286**, 229-255

Huai X., Joslin R. D. & Piomelli U. 1997 Large-eddy simulation of transition to turbulence in boundary layers. *Theoret. Comput. Fluid Dynamics* **9**, 149-163

Kachanov Y. S. 1994 Physical mechanism of laminar-boundary-layer transition. *Ann. Rev. Fluid Mech.*, **26** , 411-482

Kachanov YU. S., & Levchenko V. YA. 1984 The resonant interaction of disturbances at laminar -turbulent transition in a boundary layer. *J. Fluid Mech.* **138**, 209-247

Nagarajan, S., Ferziger, J. H. & Lele, S. K. 2004 Leading edge effects in bypass transition. *Report No.* TF-90, Stanford University

Moin P., Squites K., Cabot W., & lee S. 1991 A dynamic subgrid-scale model for compressible turbulence and scalar transport. *Phys. Fluids. A* **3** (11), 2746-2757

Spalart P. R., & Watmuff J. H. 1993 Experimental and numerical study of a turbulent boundary layer with pressure gradients. *J. Fluid Mech.* **249**, 337-371

Smagorinsky J. 1963 General circulation experiments with the primitive equations. *Mon. Weather Rev.* **91**, 99-164

White F. M. 1991 *Viscous fluid flow*, third edition, McGraw-Hill

Wray A. & Hussaini M. Y. 1984 Numerical experiments in boundary-layer stability. *Proceedings of royal society of london*, **A392** , 373-389.

Wu X., & Moin P. 2009 Direct numerical simulation of turbulence in a nominally zero-pressure-gradient flat-plate boundary layer. *J. Fluid Mech.* **630**, 5-41